A conceptual study of a high gradient trapped field magnet (HG-TFM) toward providing a quasi-zero gravity space on Earth

Keita Takahashi[1] , **Hiroyuki Fujishiro**[1] **and Mark D Ainslie**[2]

[1] Department of Physical Science and Materials Engineering, Faculty of Science and Engineering, Iwate University, Morioka 020-8551, Japan
[2] Bulk Superconductivity Group, Department of Engineering, University of Cambridge, Cambridge CB2 1PZ, United Kingdom

E-mail: s3119004@iwate-u.ac.jp and fujishiro@iwate-u.ac.jp

CrossMark

Abstract

In this work, we propose a new concept of a high gradient trapped field magnet (HG-TFM). The HG-TFM is made from (RE)BaCuO bulk superconductors, in which slit ring bulks (slit-TFMs) are tightly stacked with TFM cylinders (full-TFMs), and state-of-the-art numerical simulations were used to investigate the magnetic and mechanical properties in detail during and after magnetization. A maximum value of the magnetic field gradient product of $B_z \cdot dB_z/dz = 6040$ T^2 m^{-1} was obtained after conventional field cooled magnetization (FCM) with an applied field, B_{app}, of 10 T of the HG-TFM with 60 mm in outer diameter and 10 mm in inner diameter. This value may be the highest value ever reported compared to any other magnetic sources. The $B_z \cdot dB_z/dz$ value increased with decreasing inner diameter of the HG-TFM and with increasing B_{app} during FCM. The electromagnetic stress in the HG-TFM during the FCM process mainly results from the hoop stress along the circumferential direction. The simulations suggested that there is no fracture risk of the bulk components during FCM from 10 T in a proposed realistic configuration of the HG-TFM where both TFM parts are mounted in Al-alloy rings and the whole HG-TFM is encapsulated in a steel capsule. A quasi-zero gravity space can be realized in the HG-TFM with a high $B_z \cdot dB_z/dz$ value in an open space outside the vacuum chamber. The HG-TFM device can act as a compact and cryogen-free desktop-type magnetic source to provide a large magnetic force and could be useful in a number of life/medical science applications, such as protein crystallization and cell culture.

Keywords: bulk superconductors, trapped field magnets, high gradient magnets, finite element method, magnetic levitation, quasi-zero gravity

(Some figures may appear in colour only in the online journal)

1. Introduction

Zero gravity in space is known to be a characteristic condition in scientific research fields. Up to now, some experimental research has been carried out exploiting quasi-zero gravity conditions in the International Space Station as an environmental parameter, which focuses positively on applications related to life/medical sciences, such as protein crystallization [1] and cell culture [2] without natural convection caused by the gravitational force of the Earth. The so-called 'space biology' resulting from this research is an important developing field that could contribute significantly to the sustainable development goals.

A large magnetic field in combination with a large field gradient can provide a repulsive force against gravity on the Earth and achieve a counter-balance situation for any diamagnetic materials such as water, common metals and even cells of the human body. In 1990, magnetic levitation of diamagnetic materials such as water and plastics was first demonstrated by Beaugnon *et al* using a hybrid-type superconducting magnet (HM), in which a magnetic field gradient product, $B_z \cdot dB_z/dz$, as high as -1923 T^2 m^{-1} was applied along the vertical direction against gravity on Earth [3].

Superconducting technologies have satisfied several demands for high magnetic fields including magnetic levitation. Nikolayev *et al* summarizes the specification of existing superconducting magnets worldwide, where the highest $B_z \cdot dB_z/dz = -3000$ T^2 m^{-1} with a record-high magnetic field of 30 T has been ever achieved in a HM and superconducting coil magnet (SM) [4]. Cryo-cooled superconducting magnets without liquid helium that can generate $B_z \cdot dB_z/dz$ up to -400 T^2 m^{-1} with magnetic fields up to 10–12 T are now used practically at the laboratory scale.

The magnetic force, F_m, acting on a material increases in proportional to the magnetic field, B_z, and the magnetic field gradient, dB_z/dz, along the z-axis (upper direction) as follows,

$$F_m \propto B_z \cdot \frac{dB_z}{dz}. \tag{1}$$

To enhance F_m, there are some trends related to the magnet design, i.e. the improvement of B_z and/or dB_z/dz. One example is the gradient-type superconducting magnet developed for protein crystallization, in which an inverse coil made from Nb$_3$Sn was placed on the hybrid coil, consisting of an inner Nb$_3$Sn coil and outer NbTi coils. As a result, the magnet can generate a $B_z \cdot dB_z/dz$ as large as -1500 T^2 m^{-1} around the boundary of both coils [5]. The most significant issue is that such a comparatively large $B_z \cdot dB_z/dz$ value has been realized only in a specialized facility [4]. For practical use of a magnetic quasi-zero gravity condition on ground, it is desirable for the magnetic source to be lightweight, mobile, and cost-effective as a desktop-type apparatus, and preferably cryogen-free, i.e. operating without the need for any coolant such as liquid helium.

Large, single-grain (RE)BaCuO bulk superconductors (RE: rare earth element or *Y*) can be utilized as a compact and strong, quasi-permanent magnet [6]. Magnetic flux is trapped in bulk superconductors by a supercurrent flowing with zero-resistivity due to electromagnetic induction after applying and removing a large magnetizing field. Such (RE)BaCuO bulks with a critical temperature, T_c, over 90 K are the most promising materials to be utilized as a trapped field magnet (TFM) in a compact and desktop-type magnetic source. The record-high trapped field, 17.6 T, was achieved at the center of a two-stack GdBaCuO bulk pair magnetized by field-cooled magnetization (FCM) at 26 K using outer shrink-fit stainless steel (SS) rings [7] as well as at 23 K using SS laminations [8]. Regarding the validity of bulk TFMs magnetized by FCM, Vakaliuk *et al* indicated that the reproducibility of the trapped field can be verified experimentally under the applied field of 10 T at 50 K, but might not be proved for higher fields over $B_{app} = 14$ T [9]. The exploration of practical use of such strong TFMs can be classified into three phases: fabrication, magnetization, and applications [6, 10]. Such experimental work has showed the significant potential of such TFMs as a powerful magnetic source. However, its configuration would not be appropriate for practical use in applications, which sometimes require the large magnetic field and/or gradient product to be provided in an open space inside or outside vacuum chamber.

Recently, the authors proposed a new concept of the hybrid TFM lens (HTFML), consisting of two bulk parts: an inner bulk lens and outer bulk cylinder [11]. The diamagnetic lens effect of the inner bulk lens can concentrate the trapped field generated from the outer bulk TFM cylinder after magnetization. It was predicted numerically that an HTFML consisting of a GdBaCuO bulk lens and GdBaCuO TFM cylinder can generate a concentrated magnetic field of $B_c = 11.4$ T at 20 K that is higher than the external magnetic field of $B_{app} = 10$ T, quasi-permanently without any additional power consumption [12]. Experimental validation has proved the feasibility of the HTFML, exploiting an inner GdBaCuO bulk lens and outer MgB$_2$ TFM cylinder, in which $B_c = 3.5$ T was achieved for $B_{app} = 2.0$ T at 20 K [13]. This HTFML device suggests a new pathway to enhance the trapped field from the viewpoint of the magnetizing method in contrast to conventional approaches that depend on the superconducting properties of the bulk itself.

Additionally, in the case of the HTFML using a GdBaCuO bulk lens and GdBaCuO TFM cylinder, we showed that a magnetic field gradient product as high as $B_z \cdot dB_z/dz = -3000$ T^2 m^{-1} could be generated inside the bulk annuli under the concentrated trapped field of $B_c = 11.4$ T at 20 K, which allows for a quasi-zero gravity environment in a cost-effective and efficient way [12]. However, the HTFML device has some challenges in its construction and the magnetizing process. The temperature of the GdBaCuO bulk lens and the GdBaCuO TFM cylinder must be controlled individually during zero field-cooled magnetization (ZFCM) for the lens part and FCM for the TFM part. A special technique is required in order to control the temperature separately and the magnetization process can take several hours. Moreover, it is quite difficult to realize a room temperature bore for practical applications exploiting the advantages of the HTFML because of a narrow bore less than 10 mm in diameter in the GdBaCuO lens, which is also encapsulated in a SS holder. This does limit the effective size for practical scientific experiments.
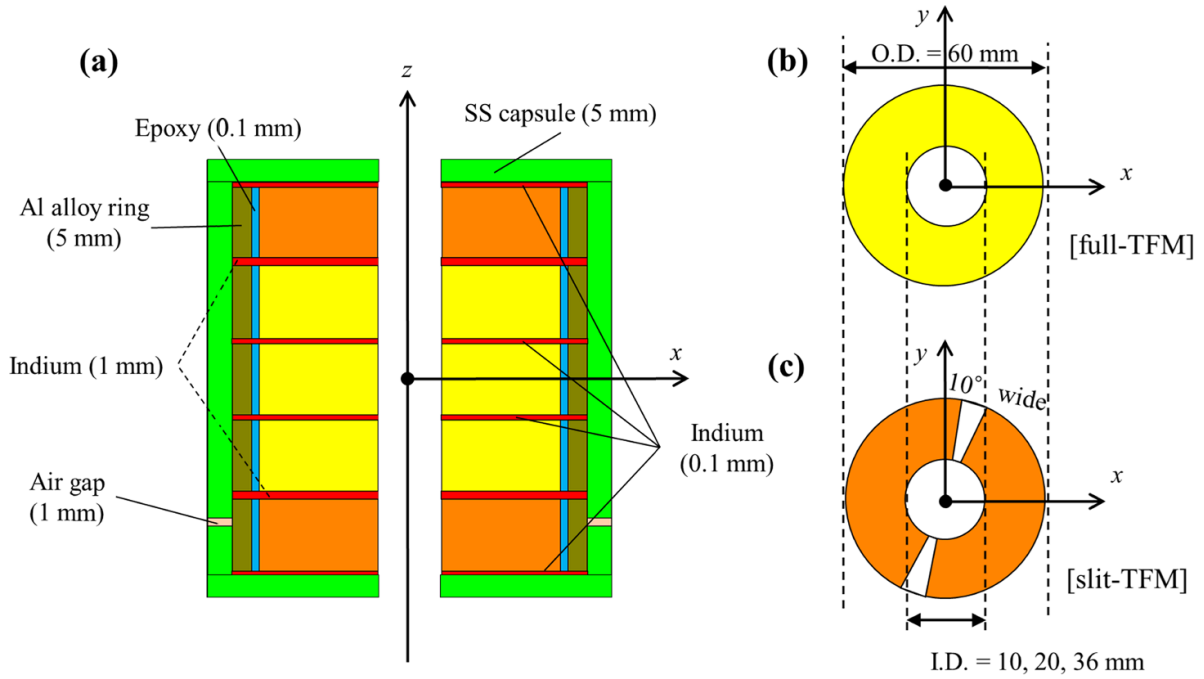
Figure 1. (a) Cross-sectional schematic of the three-dimensional numerical model of the HG-TFM, in which a conventional ring-shaped TFM cylinder, labelled 'full-TFM' (yellow), is sandwiched by two TFM cylinders with slits 10 deg. wide in the diagonal direction, labelled 'slit-TFM' (orange). The top views of the full-TFM and slit-TFM are also shown in (b) and (c), respectively.

In this study, we propose a new high gradient TFM (hereafter referred to as HG-TFM) to realize a quasi-zero gravity environment, in which slit ring bulks are combined with bulk TFM cylinders, and the magnetic properties were investigated in detail during and after magnetization using state-of-the-art numerical simulations. A maximum value of $B_z \cdot dB_z/dz = -6040$ T^2 m^{-1} was obtained after conventional FCM from $B_{app} = 10$ T at 40 K for an HG-TFM with 10 mm in inner diameter, which may be the highest value ever reported compared to any other magnetic sources. The mechanical properties of the HG-TFM were also investigated to propose a realistic configuration of the HG-TFM device reinforced by a metal support structure that is essential to prevent mechanical fracture of the bulk superconducting material during the FCM process due to its brittle, ceramic nature.

2. Numerical modeling procedure

Focusing on magnetic force applications for magnetic levitation [14–16], a higher magnetic field gradient product, $B_z \cdot dB_z/dz$, is desirable in the system as indicated by equation (1). The magnetic field gradient (dB_z/dz) term should be highly considered, as well as the trapped field (B_z) term, to improve the value of $B_z \cdot dB_z/dz$ overall.

Figure 1(a) presents a cross-sectional schematic of the three-dimensional numerical model of the HG-TFM, in which a conventional ring-shaped TFM cylinder, labeled 'full-TFM', is sandwiched by two TFM cylinders with slits 10 deg. wide in the diagonal direction, labeled 'slit-TFM'. Figures 1(b) and (c) show the top views of the full-TFM and slit-TFM, respectively. The outer diameter (O D) of the HG-TFM is 60 mm and the
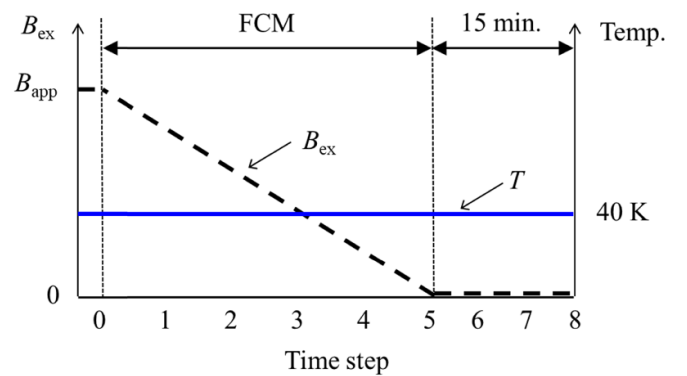

Figure 2. Magnetizing sequence for FCM of the HG-TFM, which is the same as that for a conventional TFM. The external field, B_{ex}, is decreased linearly at a ramp rate of -0.222 T min^{-1} from $B_{app} = 3$, 5 or 10 T at a constant temperature at 40 K.

inner diameter (I D) is assumed to be either 10, 20 or 36 mm for both TFM components. The height (H) of the full-TFM is 48 mm, for which three ring-shaped bulks 16 mm in H are stacked, and each of the slit-TFMs are 16 mm in H. In the model, the height of the full-TFM is determined so that the trapped field capability to be 10 T for the HG-TFM with wider I D = 36 mm and is fixed temporarily for the comparison with various I D cases. The number of layers of the full-TFM can be reduced within the capability required in the device. Each bulk is mounted separately in an Al-alloy ring 5 mm in thickness (O D = 70 mm, I D = 60 mm, $H = 16$ mm) adhered by a thin layer of epoxy resin. A thin indium sheet layer (0.1 or 1 mm in thickness) is inserted between each bulk to reproduce the boundary condition between each bulk in the realistic HG-TFM. A

Table 1. Numerical fitting parameters for the assumed $J_c(B)$ characteristics of the GdBaCuO bulk used in equation (3), where the β value is adjusted to reproduce the experimental result for the trapped field [12].

T (K)	J_{c1} (A m^{-2})	B_L (T)	J_{c2} (A m^{-2})	B_{max} (T)	α	β
40	3.5×10^9	0.9	2.7×10^9	6.0	0.8	0.50
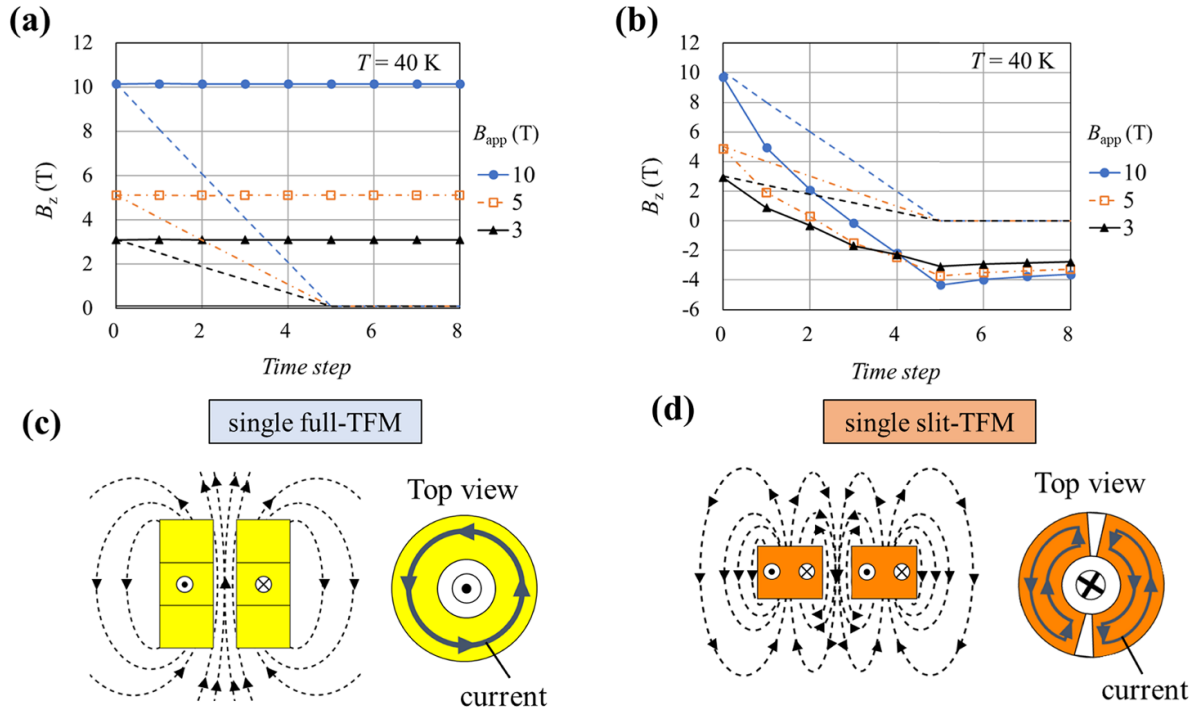
Figure 3. The time step dependence of the magnetic field, B_z, during FCM from $B_{app} = 3$, 5 and 10 T at 40 K at the center of (a) the single full-TFM (I D = 10 mm, O D = 60 mm, H = 48 mm) and (b) the single slit-TFM (I D = 10 mm, O D = 60 mm, H = 16 mm, slit 10 deg. wide). The schematic view of the magnetic flux distribution and induced current direction in (c) the single full-TFM and (d) the single slit-TFM.

solenoid coil of 170 mm in O D, 120 mm in I D and 200 mm in H is used to apply the magnetic field for the magnetization process (not shown in figure 1). As described earlier, appropriate mechanical reinforcement must be considered for the bulks due to their brittle, ceramic nature for improving the reliability of the magnetization process and the device itself. Several studies have investigated the fracture behavior of the bulk TFMs, which has a high risk of occurring under FCM from applied fields over 10 T at temperatures lower than 50 K, in particular [17–19]. As shown in figure 1(a), the model represents a realistic experimental setup for the mechanical reinforcement of the bulk magnets, which will be performed in the near future, employing outer Al-alloy rings and an outer SS capsule of 5 mm in thickness that can provide a compressive stress over -100 MPa when cooling from room temperature to the operating temperature to perform FCM. The mechanical reinforcement could endure up to $B_{app} = 10$ T in actual FCM experiments [20, 21].

Figure 2 presents the magnetizing sequence for FCM of the HG-TFM, which is the same as that for a conventional TFM. The external field, B_{ex}, is decreased linearly at a ramp rate of -0.222 T min^{-1}. from $B_{app} = 3$, 5 or 10 T at a constant temperature at 40 K. Once the external field is ramped down
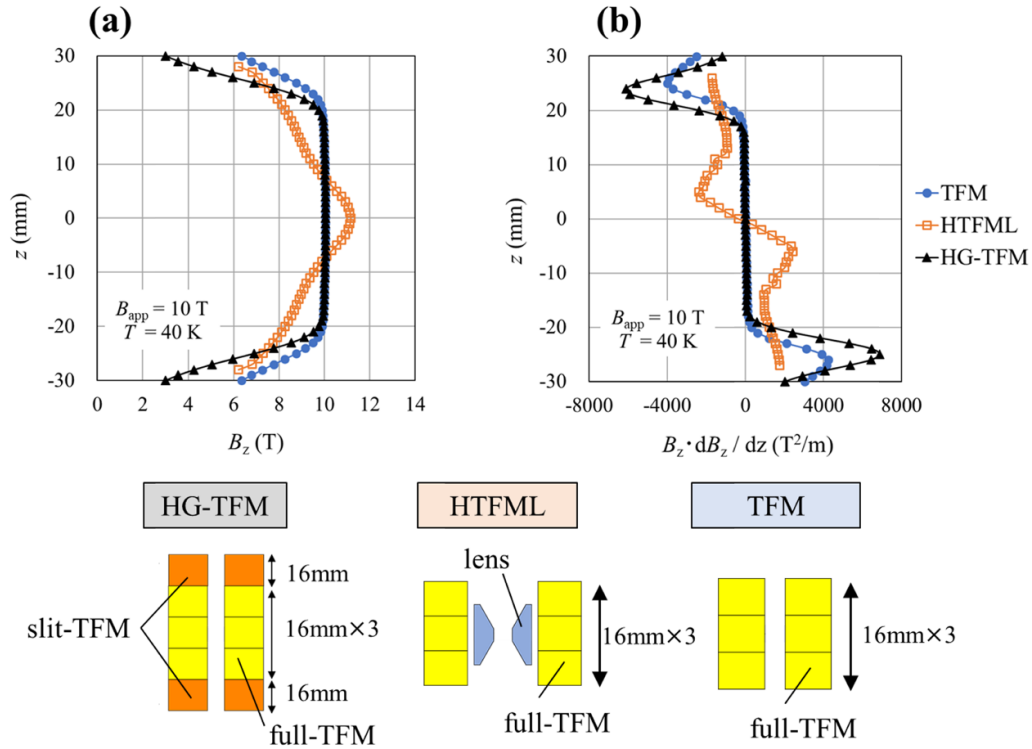
to 0 T for step 5, the static magnetic field 15 min later (for step 8) is then referred to as the trapped field value, B_T. Only the z-component is considered for magnetic levitation because gravity acts along the z direction. The electromagnetic phenomena of the bulk superconductor during the magnetization process are analyzed using the commercial software, Photo-EDDY (Photon Ltd, Japan).

The nonlinear electrical property of the bulk superconductor is derived from the E–J power law as follows,

$$E = E_c \left(\frac{J}{J_c} \right)^n, \tag{2}$$

where $E_c = 10^{-4}$ V m^{-1} is the characteristic electrical field, $n = 20$ is an appropriate power-law exponent for GdBaCuO bulk, and J_c is the critical current density. The realistic $J_c(B)$ characteristics, including the fish-tail effect under certain magnetic fields, can be represented by the following equation proposed by Jirsa *et al* [22],

$$J_c(B) = \beta \cdot \left\{ J_{c1} \exp\left(-\frac{B}{B_L}\right) + J_{c2} \frac{B}{B_{max}} \exp\left[\frac{1}{\alpha}\left(1 - \left(\frac{B}{B_{max}}\right)^\alpha\right)\right] \right\}, \tag{3}$$

Figure 4. Numerical results for (a) the magnetic field, B_z, and (b) the magnetic field gradient product, $B_z \cdot dB_z/dz$, after magnetization with $B_{app} = 10$ T at 40 K along the z-axis inside the bulk annuli, comparing three types of TFMs: the HG-TFM, the HTFML and a conventional ring-shaped TFM (single full-TFM).

where each relevant parameter, J_{c1}, B_L, J_{c2}, B_{max}, and α are fitted from the experimental results for a GdBaCuO bulk reported by Kii *et al* [23]. The fitting coefficient, β, is employed so as to modify the deviation from the actual trapped field value (obtained experimentally) after FCM, particularly at temperatures lower than 50 K [12]. The parameters assumed for the GdBaCuO bulk material for equation (3) are summarized in table 1.

3. Electromagnetic analysis results

Before describing the mechanism of the HG-TFM in detail, the electromagnetic properties of each key component of the HG-TFM—the single full-TFM and the single slit-TFM—were investigated. Figures 3(a) and (b), respectively, show the time step dependence of the magnetic field, B_z, during FCM from $B_{app} = 3$, 5 and 10 T at 40 K at the center of the single full-TFM (I D = 10 mm, O D = 60 mm, $H = 48$ mm) and the single slit-TFM (I D = 10 mm, O D = 60 mm, $H = 16$ mm, slit 10 deg. wide). For the single full-TFM case shown in figure 3(a), the final trapped field, B_T, after FCM was almost equivalent to each B_{app} because of partial magnetization within the full capability of the full-TFM, which also enables the generation of a comparatively homogeneous magnetic field inside the bulk bore. Such a high field is realized by an induced supercurrent flowing inside the full-TFM as depicted. Nowadays, it is estimated that the trapped field capability for a disk-shaped bulk pair (O D = 24 mm, $H = 24$ mm) could be over 20 T, based on

current state-of-the-art $J_c(B, T)$ characteristics [8]. The schematic view of the magnetic flux distribution and induced current direction in the single full-TFM is shown in figure 3(c), in which the conventional magnetic flux lines can be seen.

In the single slit-TFM case shown in figure 3(b), when B_{ex} decreased linearly, the B_z steeply decreased and became a negative value. Finally, the B_z value took a negative maximum at step 5 and then slightly recovered to the final B_T value because of the non-linear electrical property of bulk superconductor (see equation (2)). At step 8, $B_T = -2.8, -3.3, -3.6$ T values were obtained at the center of the single slit-TFM for $B_{app} = 3$, 5 and 10 T, respectively. Figure 3(d) also shows the schematic view of the magnetic flux distribution and induced current direction in the single slit-TFM. An induced current flows counterclockwise in each piece separated by the slits, which is the same direction with the full-TFM. However, the downward ($-z$-direction) magnetic flux would penetrate through the slit gap and exist even inside the central bore to build the magnetic loop in each piece of the slit-TFMs, which becomes the opposite direction to that generated by the single full-TFM ($+z$-direction). The HG-TFM then provides a large magnetic field gradient around the interface between the full-TFM with upward magnetic flux lines and the slit-TFM with downward magnetic flux lines.

Figures 4(a) and (b), respectively, show a comparison of the numerical results for the magnetic field, B_z, and the magnetic field gradient product, $B_z \cdot dB_z/dz$, after magnetization with $B_{app} = 10$ T at 40 K along the z-axis inside the bulk annuli, comparing three types of TFMs: the HG-TFM, the HTFML
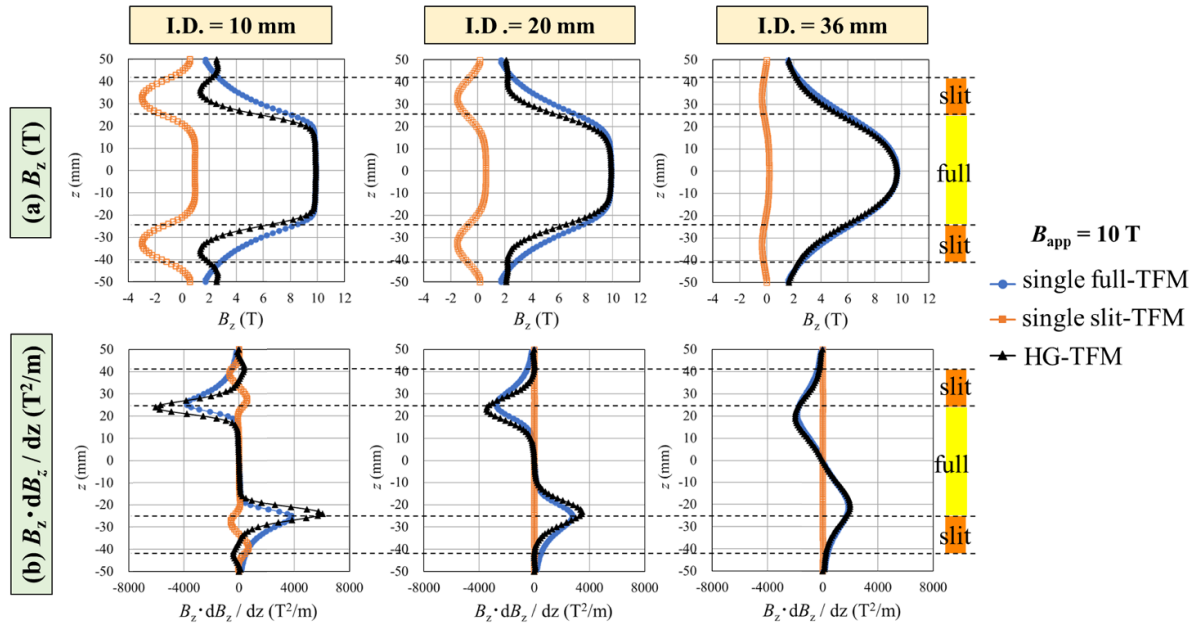
Figure 5. (a) The magnetic field, B_z, and (b) the magnetic field gradient product, $B_z \cdot dB_z/dz$, profiles of the HG-TFM with inner bores of I D = 10, 20 and 36 mm along the z-direction inside the bulk bore after FCM from $B_{app} = 10$ T at 40 K, compared with those of a single full-TFM (-24 mm $\leqslant z \leqslant 24$ mm) and single slit-TFM pair ($\pm z = 25 \sim 41$ mm).

and a conventional ring-shaped TFM (single full-TFM). The dimensions of each TFM are shown in the figure, where the dimensions of the full-TFM part were assumed to be identical for each case (I D = 10 mm, O D = 60 mm, $H = 48$ mm). The dimensions of the magnetic lens for the HTFML can be referred to elsewhere [12]. In figure 4(a), the trapped field, B_z, at the center ($z = 0$ mm) of the HG-TFM and full-TFM should be comparable with the applied field of $B_{app} = 10$ T. On the other hand, for the HTFML exploiting the diamagnetic lens effect, B_z can be concentrated into the bulk annuli, in which a concentrated trapped field of $B_c = 11.0$ T was achieved at 40 K at $z = 0$ mm. In figure 4(b), the HG-TFM shows the highest $B_z \cdot dB_z/dz$ value of -6040 T^2 m^{-1} at the boundary between each TFM part, $z = 24$ mm, which is remarkably superior than the other two types of TFM. In this sense, to improve the magnetic force efficiently, it would be more desirable to control the magnetic field gradient (dB_z/dz) profile by focusing on the gradient itself rather than improving the trapped field (B_z). One significant advantage of the HG-TFM is that its superior magnetic properties could be realized using a conventional FCM process at one temperature and without any additional costs, except for the slit-TFM. Note again that figure 4 is an example assuming a narrow 10 mm bore in inner diameter for each system. The magnetic properties of the HG-TFM would change depending on the shape of the bulk material (O D, I D, H, slit angle and so on) and the conditions of the magnetization process, such as the magnetizing temperature and B_{app}.

Figures 5(a) and (b), respectively, show the magnetic field, B_z, and the magnetic field gradient product, $B_z \cdot dB_z/dz$, profiles of the HG-TFM with inner bores of I D = 10, 20 and 36 mm along the z-direction inside the bulk bore after FCM from $B_{app} = 10$ T at 40 K, compared with those of a single full-TFM (-24 mm $\leqslant z \leqslant 24$ mm) and single slit-TFM pair

($\pm z = 25 \sim 41$ mm). In figure 5(a), the slit-TFM pair with a narrower bore of I D = 10 mm generates a higher negative trapped field ($= -3$ T) over a wider area at $\pm z = 20 \sim 40$ mm, which is effective for improving the HG-TFM performance with a larger magnetic field gradient. The negative trapped field of the single slit-TFM pair decreased with increasing I D value and there is no remarkable negative value for I D = 36 mm. On the other hand, for the cases of the full-TFM and HG-TFM, the B_z profile becomes broad with increasing I D value and the shape of the trapped field profile no longer varies between the full-TFM and HG-TFM with I D = 36 mm. Since B_z decays significantly with distance outside of the TFM, i.e. at $\pm z \geqslant 24$ mm, there is less, or no magnetic flux controlled in the HG-TFM with wider I D = 36 mm.

In figure 5(b), for the HG-TFM, the peak value of $B_z \cdot dB_z/dz$ was enhanced with decreasing I D at the boundary position between each TFM around $\pm z = 24$ mm due to the presence of the slit-TFM. A maximum $B_z \cdot dB_z/dz$ value of 6040 T^2 m^{-1} was achieved for I D = 10 mm, which is larger than that for the full-TFM (-3790 T^2 m^{-1}). It should be noted that a $B_z \cdot dB_z/dz$ value as large as -1400 T^2 m^{-1} along the $+z$-direction of the vertical magnet is required to levitate a diamagnetic water drop in air [24]. In this sense, the effective volume for magnetic levitation can be estimated to be $+z = 19$–30, 17–30 and 13–27 mm inside the bore of the HG-TFM with I D = 10, 20 and 36 mm, respectively. For protein crystallization in a diamagnetic solution, a larger $B_z \cdot dB_z/dz$ value of -4450 T^2 m^{-1} is required to realize an apparent zero-gravity condition without buoyancy flow, which is much higher than that estimated numerically [25]. For realizing a higher field gradient product, the HG-TFM with a narrower inner bore is desirable, leading to a trade-off between field gradient product and effective volume.
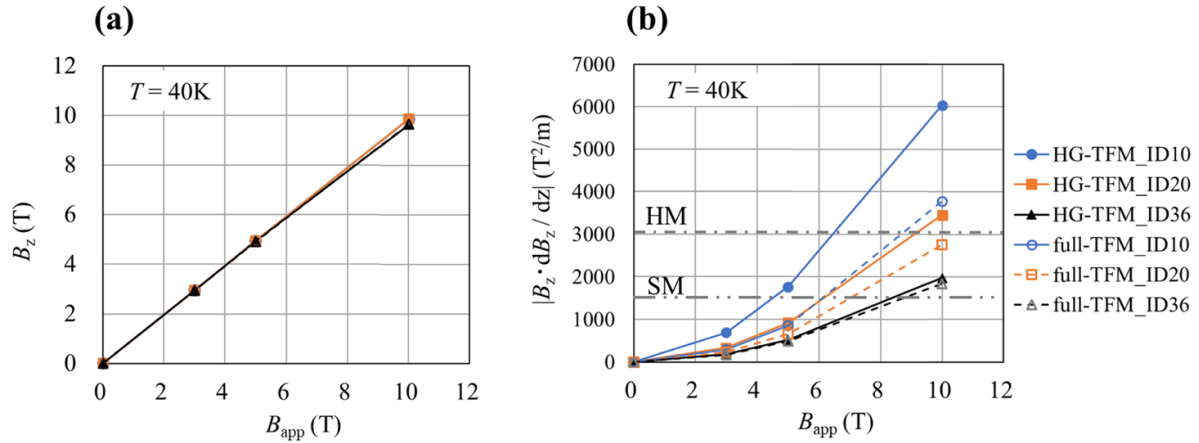
Figure 6. (a) The final trapped field, B_T (= B_z at step 8), at the center ($x = y = z = 0$) and (b) the maximum field gradient product, $|B_z \cdot dB_z/dz|$, at the boundary position between the full and slit-TFMs of the HG-TFM, as a function of B_{app} for various I D cases. The results are compared to that of the full-TFM cases and other large-scale magnets: superconducting magnets (SM), and hybrid-type superconducting magnets (HM).

Figures 6(a) and (b) summarize the final trapped field, B_T (= B_z at step 8), at the center ($x = y = z = 0$) and the maximum field gradient product, $|B_z \cdot dB_z/dz|$, around the boundary position between the full and slit-TFMs of the HG-TFM, as a function of B_{app} for various I D cases. The results for the full-TFM cases are also shown for reference. In figure 6(a), the trapped field capability is equivalent for all cases; thus, the relation $B_T = B_{app}$, is established based on the typical FCM process. However, for the magnetic field gradient product shown in figure 6(b), the HG-TFM would work more effectively for B_{app} higher than 5 T and for narrower bores smaller than I D = 20 mm compared to the full-TFM. Table 2 summarizes the maxima of the magnetic properties for each case including the HG-TFM, HTFML and full-TFM, extracted from figures 4 and 6. The HG-TFM with I D = 10 mm would provide a maximum $|B_z \cdot dB_z/dz| = 6040$ T m^{-2} when $B_T = 10$ T at 40 K, which may be the record-high value compared to that of other large-scale magnets: SM ~ 1500 T m^{-2}, and HM ~ 3000 T m^{-2} using liquid helium, shown in figure 6(b) [4, 26].

In most related studies, based on apparatus using a permanent magnet with a magnetic field ~ 1 T, the magneto-Archimedes method must be exploited to reduce the required magnetic force using a paramagnetic medium solution [27, 28]. The HG-TFM no longer needs such a method, and consequently, can provide simpler, medium-free operation with air or water. These advantages of the HG-TFM can provide the versatility of a quasi-zero gravity space as a desktop-type magnetic source for magnetic levitation processing, which enables the suppression of gravity-induced convection in a wide range of potential industrial applications such as protein crystallization and cell culture [1, 2]. It should be noted that $B_z \cdot dB_z/dz$ values of 1980 and 2760 T^2 m^{-1} can be achieved after FCM from $B_{app} = 10$ T even for the single full-TFM with I D = 36 and 20 mm (without the slit-TFM), respectively, as shown in table 2, which are higher than that achieved by SMs [4]. These results suggest that the single full-TFM can be also applicable for quasi-zero gravity in the open

space outside the vacuum chamber with a range of 15–30 mm in diameter. There is a limit for the enlargement of the space in the bore because it is difficult to fabricate good quality bulks >60 mm in O D, resulting in a narrower bore compared to that of SMs.

In our previous work [12], where the mechanism of magnetic levitation in the quasi-zero gravity space is explained in detail, it was highlighted that a large magnetic field gradient product up to 3000 T^2 m^{-1} of that particular HTFML design could be highly applicable to magnetic separation. Regarding the effectiveness of the magnetic force for crystal growth, it is shown elsewhere that the magnetic force affects several features: the magnetic field orientation, convection control, reduction of sedimentation and so on [14]. However, there are no theoretical rules yet regarding how the magnetic force works during the process and it differs between the target materials used. Thus, appropriate design of the I D of the HG-TFM needs to be explored as related to the particular application, where the magnetic force profile in the HG-TFM could be correlated with the quality of the resultant crystallization.

4. Mechanical stress analysis results

The mechanical fracture of bulk superconductors has been reported in several studies, where a crack might occur along the circumferential direction mainly due to the hoop stress induced during FCM from applied fields over 10 T at temperatures below 50 K [17–19]. To date, to prevent such mechanical fracture during magnetization, mechanical reinforcement has been usefully applied using glass fiber reinforced epoxy resin [29] or shrink-fit steel [7]. We also proposed a new hat structure of an outer metal reinforcement ring based on the results of mechanical stress simulations, in which a large (RE)BaCuO ring-shaped bulk (I D = 36 mm, O D = 60 mm, $H = 20$ mm) was experimentally confirmed to endure FCM from 10 T without fracture [20]. For the HTFML consisting of a (RE)BaCuO lens and (RE)BaCuO TFM cylinder,

Table 2. Numerical results of maxima of the magnetic properties for each case including the HG-TFM, HTFML and full-TFM magnetized at 40 K, extracted from figures 4 and 6.

	HG-TFM			HTFML
Bulk I D (mm)	10	20	36	10
B_z (B_{app}) (T)	10 (10)	10 (10)	9.8 (10)	11 (10)
$\|B_z \cdot dB_z/dz\|$ ($T^2\ m^{-1}$) (single full-TFM)	6040 (3790)	3460 (2760)	1980 (1850)	2430 (1850)
Magnetization		FCM		ZFCM + FCM
Temperature (K)		40		

the mechanical properties have been analyzed during the magnetizing process from B_{app} = 10 T [30], in which the necessity of adequate mechanical reinforcement was strongly suggested, at least for the GdBaCuO TFM cylinder, but possibly the magnetic lens as well. It is also necessary to investigate the mechanical properties of the present HG-TFM as well during FCM, where the full-TFM part is tightly sandwiched by the slit-TFM pair.

After calculating the trapped field profile shown in the previous section, the nodal force was then imported into another software package, Photo-ELAS (Photon Ltd., Japan), for calculating the electromagnetic stress on each mesh element of the bulk TFMs during magnetization, which enables us to assess the reliability of the HG-TFM in terms of the mechanical reinforcement method.

Elastic behavior in an isotropic material can be expressed by Hooke's law, in which the stress tensor, σ_{ij}, is linearly proportional to the strain tensor, ε_{ij}, as follows

$$\sigma_{ij} = \lambda \cdot \varepsilon_{kk} \cdot \delta_{ij} + 2G \cdot \varepsilon_{ij}, \tag{4}$$

$$\lambda = \frac{E \cdot \nu}{(1+\nu)(1-2\nu)}, \tag{5}$$

$$G = \frac{E}{2(1+\nu)}, \tag{6}$$

where λ and G represent Lame's constants, δ_{ij} is the Kronecker delta function, E_Y is the Young's modulus, and ν is the Poisson ratio. The mechanical parameters, E_Y and ν, for each component of the HG-TFM are summarized in table 3, which are assumed in the simulation to be isotropic and in the elastic region. Note that all components, including the epoxy resin, indium and air gap, as shown in figure 1, were included in the modeling of the HG-TFM, which should be considered for the accurate prediction of the mechanical behavior [31].

Figures 7(a) and (b) show a contour map of the Von Mises stress, σ_{VM}, and the electromagnetic hoop stress along the *y*-direction, σ_{YY}, respectively, calculated for the full-TFM part of the HG-TFM with inner diameters of I D = 10, 20 and 36 mm, just after FCM from 10 T (step 5). In figure 7(a), the σ_{VM} value, which is a scalar quantity, represents the total value of the mechanical stresses including all directions. Compared with the maximum σ_{YY} value shown in figure 7(b), which is close to the maximum σ_{VM} value of 90 MPa around the inner periphery of the full-TFM part, it was found that the

Table 3. Assumed mechanical parameters (E_Y: Young's modulus and ν: Poisson ratio) for numerical stress analysis of the HG-TFM shown in figure 1 [20, 31].

|	E_Y (GPa)	ν
(RE)BaCuO bulk	100	0.33
Epoxy resin	3.0	0.37
Al alloy (A7075-T6)	78	0.34
Indium	12.7	0.45
SS 304	193	0.28

main component of the electromagnetic stress results from the hoop stress along the *y*-direction in the full-TFM part. The maximum σ_{YY} value was almost independent of the bore size because the trapped field is equivalent for each HG-TFM with different bore sizes as shown in figure 6(a). These numerical results for the stress profile are similar to that reported for the annular (RE)BaCuO bulk magnet system (full-TFM) for an NMR spectrometer [21], in which an electromagnetic hoop stress about 100 MPa was generated at the inner peripheral region of the annular bulks reinforced by a similar structure. This means that the present reinforcement technique would work even for the present HG-TFM system. Considering the compressive stress of −100 MPa from the reinforcement by the Al-alloy rings and the SS capsule during the cooling process before FCM, the maximum total stress would be less than the fracture strength of typical Ag-doped (RE)BaCuO bulks of 50–70 MPa [32]. As a result, the full-TFM part should be appropriately reinforced and not break [21].

Figures 8(a)–(c) show the contour map of the Von Mises stress, σ_{VM}, the electromagnetic hoop stress along the *y*-direction, σ_{YY}, and the electromagnetic radial stress along the *x*-direction, σ_{XX}, respectively, for the slit-TFM pair of the HG-TFM with inner diameters of I D = 10, 20 and 36 mm, just after FCM from 10 T. For the case of I D = 10 mm, a maximum Von Mises stress of σ_{VM} = 54 MPa exists at the surfaces of the slit-TFM pair facing the full-TFM part. The σ_{XX} profile for each I D, as shown in figure 8(c), is similar to that for σ_{VM}. On the other hand, the σ_{YY} contribution to the Von Mises stress, as shown in figure 8(b), is relatively small. These results suggest that the main component of the electromagnetic stress results from the electromagnetic radial stress along the *x*-direction, σ_{XX}, in the case of I D = 10 mm and I D = 20 mm. However, for the wider I D = 36 mm, the electromagnetic stress mainly results from the hoop stress along the *y*-direction, σ_{YY}. Since an induced current flows in two regions
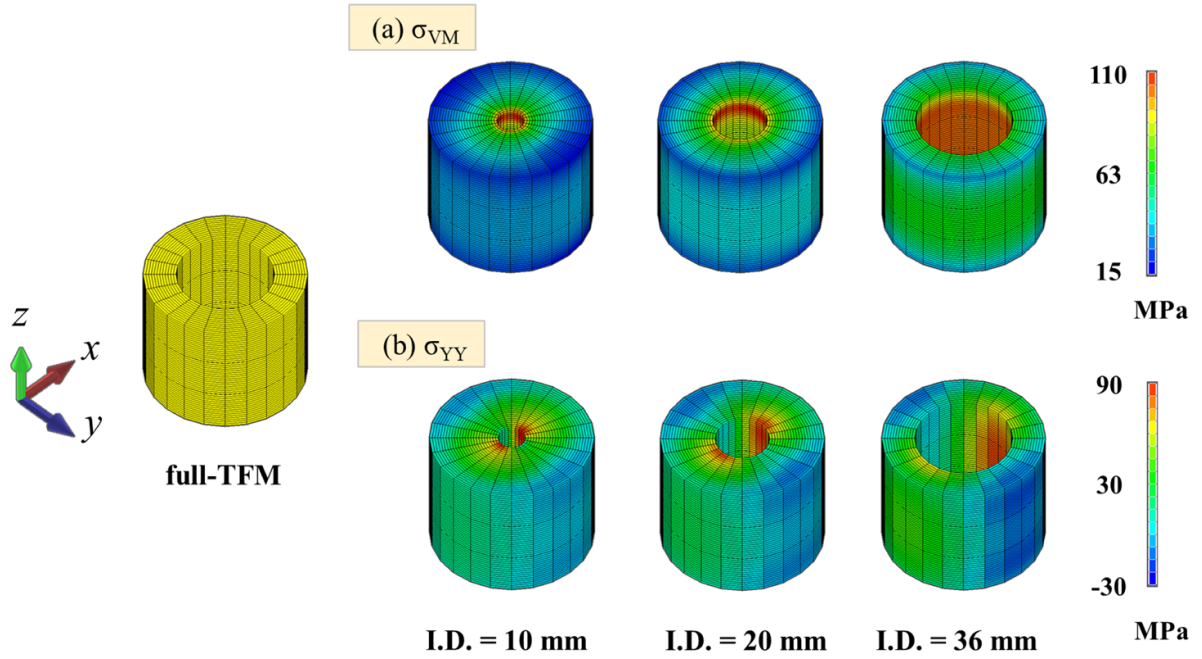
Figure 7. Contour map of (a) the Von Mises stress, σ_{VM}, and (b) the electromagnetic hoop stress along the *y*-direction, σ_{YY}, calculated for the full-TFM part of the HG-TFM with inner diameters of I D = 10, 20 and 36 mm, at step 5 just after FCM from 10 T.
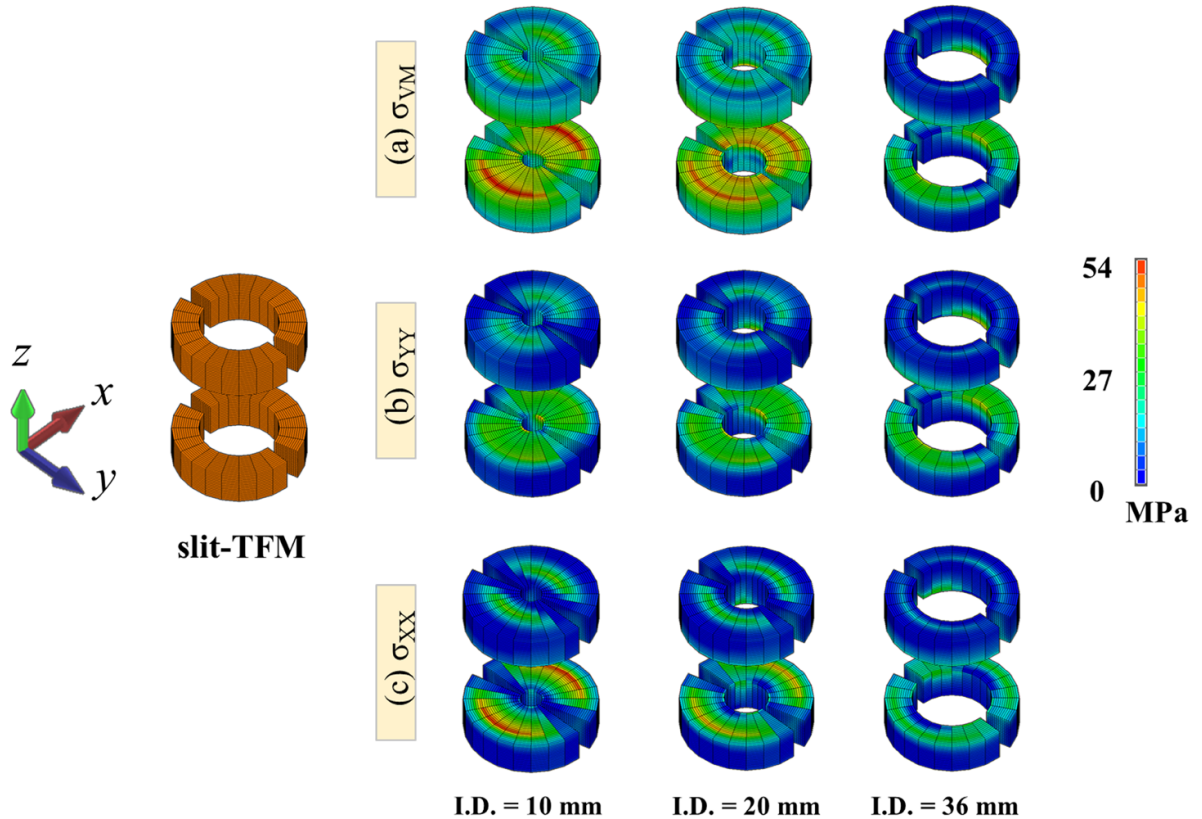
Figure 8. Contour map of (a) the Von Mises stress, σ_{VM}, (b) the electromagnetic hoop stress along the *y*-direction, σ_{YY}, and (c) the electromagnetic radial stress along the *x*-direction, σ_{XX}, for the slit-TFM pair of the HG-TFM with inner diameters of I D = 10, 20 and 36 mm, just after FCM from 10 T.

in the slit-TFM independently due to the existence of slits, the resultant trapped field and the mechanical stress become lower, compared to the full-TFM, even if the slit-TFM is magnetized by FCM from 10 T.

During the magnetization of the HG-TFM exploiting slit-TFMs stacked on the full-TFM, an extra stress component may be generated due to the repulsive force between each TFM part. Figure 9(a) shows a cross-sectional contour map
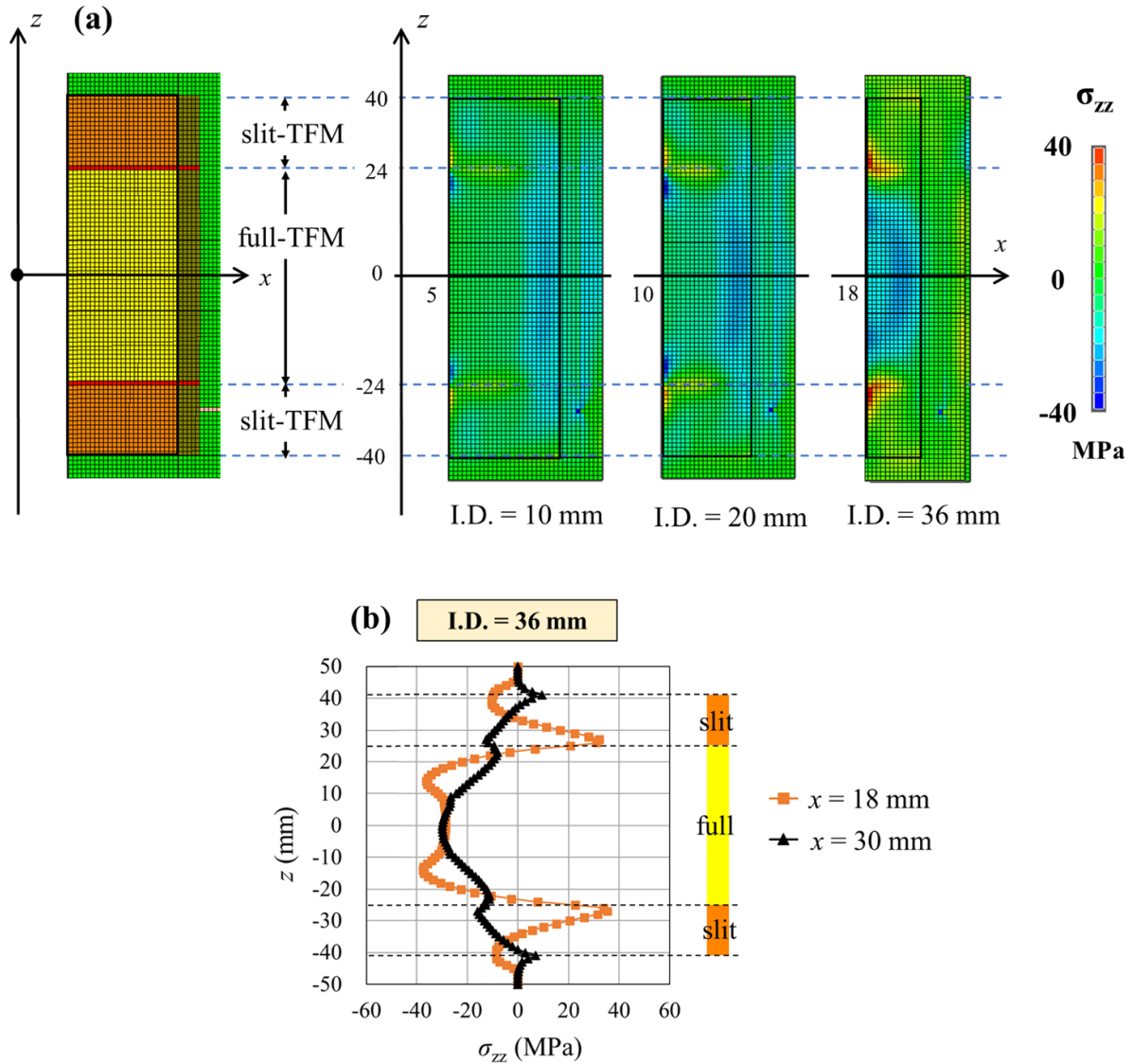
Figure 9. (a) Cross-sectional contour map of the electromagnetic stress along the vertical direction, σ_{ZZ}, for the HG-TFM with various inner diameters, just after the FCM process from 10 T. (b) The σ_{ZZ} distribution along the z-direction at the inner periphery ($x = 18$ mm) and at the outer periphery ($x = 30$ mm) for the HG-TFM with I D = 36 mm, extracted from (a).

of the electromagnetic stress along the vertical direction, σ_{ZZ}, for the HG-TFM with various inner diameters, just after the FCM process from 10 T. The positive σ_{ZZ} value is concentrated mainly in the inner periphery of the slit-TFM facing the full-TFM, and the magnitude of σ_{ZZ} increases with increasing I D These results suggest that a repulsive force exists in this region. However, the positive σ_{ZZ} region vanishes at the outer interface of the slit-TFM facing the full-TFM ($z = \pm24$ mm, $-15 \leqslant x \leqslant 30$ mm for I D = 36 mm case), which indicates the possibility of an attractive force or very small repulsive force there. Figure 9(b) shows the σ_{ZZ} distribution along the z-direction at the inner periphery ($x = 18$ mm) and at the outer periphery ($x = 30$ mm) for the HG-TFM with I D = 36 mm, which were extracted from figure 9(a). At the inner periphery, the σ_{ZZ} value changes from positive to negative around the interface ($z = \pm24$ mm). These results indicate that a repulsive force exists at the inner interface. On the other hand, at the outer periphery, the σ_{ZZ} value is negative and continuous

for both the slit-TFM and full-TFM, suggesting that an attractive magnetic force might exist at the outer interface. Similar trends were also observed for the HG-TFM for I Ds = 10 and 20 mm.

Figure 10(b) shows a contour map of the final trapped field, B_T, of the HG-TFM with I D = 20 mm after FCM from 10 T. It should be noted that a trapped field along the $+z$-direction exists at the periphery of the slit-TFM (region A), which has a similar B_T strength of 10 T as for the full-TFM. These results suggest that 'region A' is magnetically attracted to the magnetized full-TFM. On the other hand, there exists little field trapped downward along the z-direction in the inner periphery region of the slit-TFM ('region B'). These results indicate that a repulsive magnetic force exists in the counter side in the full-TFM, which can be understood well from the schematic view of the magnetic flux lines in figure 10(a).

Figure 10(a) shows a schematic view of the magnetic flux profile for the HG-TFM after FCM. To understand the
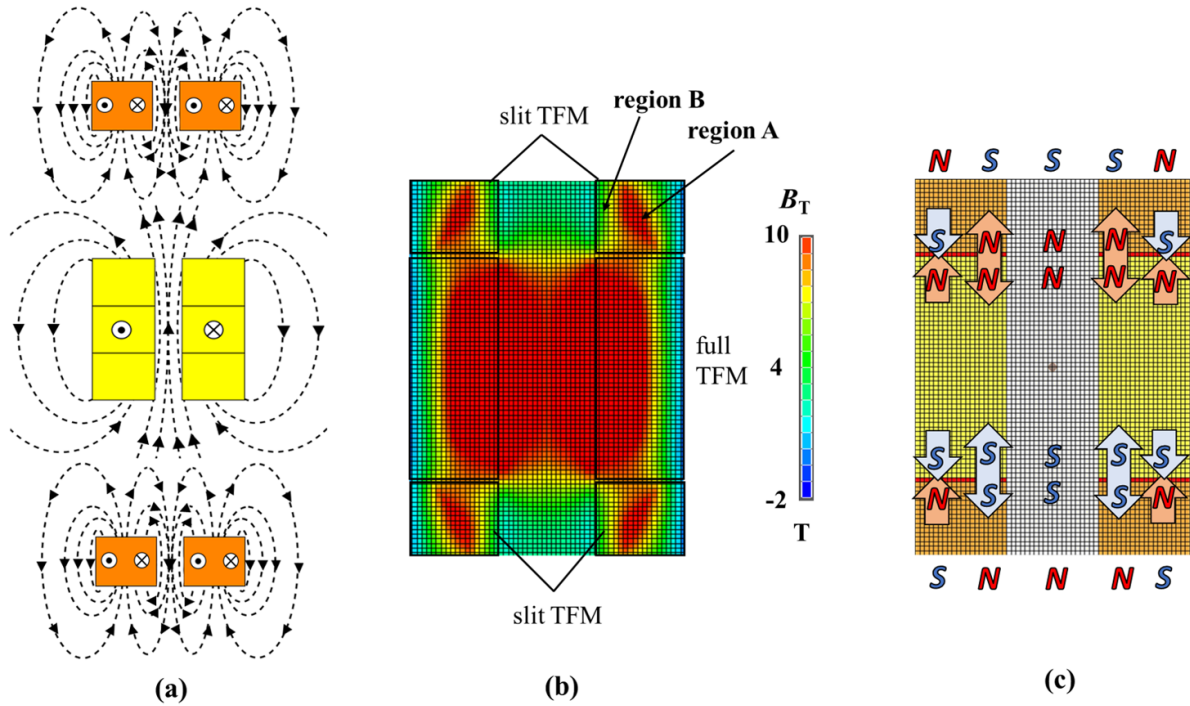
Figure 10. (a) Schematic view of the magnetic flux profile for the HG-TFM after FCM. (b) Contour map of the final trapped field, B_T, of the HG-TFM with I D = 20 mm after FCM from 10 T. (c) The effective magnetic poles of the HG-TFM after FCM. The outer periphery region (region A) and inner periphery region (region B) of the slit-TFM can be considered as opposing magnetic poles.

distribution of the magnetic flux lines at the interface visually, the full-TFM and the slit-TFM pair are placed at a distance. It can be confirmed visually that the magnetic flux lines co-exist at the interface and form the superposition of the magnetic fields that is destructive around the central bore or constructive around the bulk periphery.

Let us describe these results using a magnetic pole model. Figure 10(c) shows the effective magnetic poles of the HG-TFM after FCM, which presents the mechanism of the larger magnetic gradient of the HG-TFM. The outer periphery region (region A) and inner periphery region (region B) of the slit-TFM can be considered as opposing magnetic poles. As a result, region A is attractive (an N–S or S–N pair) and region B is repulsive (N–N or S–S pair) with respect to the magnetized full-TFM at the interface. Since both TFM parts are mounted in an Al-alloy ring and the whole HG-TFM is encapsulated in an SS capsule, σ_{ZZ} acts as a compressive stress, and that maxima is around 50 MPa for the full-TFM and 35 MPa for slit-TFM in the HG-TFM with I D = 36 mm. However, in the narrower bore cases, I D = 10 and 20 mm, σ_{ZZ} decreases despite the superior $B_z \cdot dB_z/dz$ performance. In any case, there is little fracture risk due to the compressive stress for the HG-TFM during FCM from 10 T, since the compressive fracture strength of (RE)BaCuO bulk is about one order of magnitude higher than the tensile mechanical strength [33].

5. Conclusion

We have proposed a new concept of a HG-TFM. The HG-TFM is made from (RE)BaCuO bulk superconductors to realize a quasi-zero gravity space using magnetic force, in which a slit ring bulk (slit-TFM) was tightly stacked with a TFM cylinder (full-TFM). State-of-the-art numerical simulations were used to investigate the magnetic and mechanical properties detail during and after magnetization. The important results and conclusions in this study are summarized as follows.

(a) A maximum value of the magnetic field gradient product of $B_z \cdot dB_z/dz = -6040$ T^2 m^{-1} was obtained after conventional FCM from $B_{app} = 10$ T of the HG-TFM with a 60 mm outer diameter and 10 mm inner diameter. This value may be the highest ever reported compared to any other magnetic sources. The superiority of the HG-TFM is the easier magnetization process including a single temperature and a simpler construction without any additional cost, but also the higher $B_z \cdot dB_z/dz$ can be provided in an open space outside the vacuum chamber.

(b) The $B_z \cdot dB_z/dz$ value increased with decreasing inner diameter of the HG-TFM and with increasing applied field, B_{app}, during FCM. Even if the inner diameter of the HG-TFM is 36 mm, a $B_z \cdot dB_z/dz$ value of 1980 T^2 m^{-1} can be achieved, which is slightly higher than 1850 T^2 m^{-1} for the single full-TFM case.

(c) The electromagnetic stress during the FCM process was also investigated to analyze the mechanical behavior of HG-TFM device. The electromagnetic stress in the HG-TFM device during the FCM process mainly results from the hoop stress along the *y*-direction, σ_{YY}, for the full-TFM.

(d) The outer and inner periphery regions of the slit-TFM can be considered as opposing magnetic poles. The outer

periphery region is attractive (N–S or S–N pair) and the inner periphery region is repulsive (N–N or S–S pair) with respect to the magnetized full-TFM at the interface. However, it was confirmed that there is little fracture risk for the bulks during FCM from 10 T in the proposed realistic configuration of the HG-TFM, where both TFM parts are mounted in Al-alloy rings and the whole HG-TFM is encapsulated in an SS capsule.

(e) A quasi-zero gravity space can be realized using the HG-TFM with its large $B_z \cdot dB_z/dz$ value in an open space outside the vacuum chamber even without the magneto-Archimedes method. The HG-TFM device is a compact and cryogen-free desktop-type magnetic source to provide a large magnetic force and can be applicable to scientific research, such as in the life/medical sciences for protein crystallization and cell culture.

Acknowledgments

ORCID iDs

Keita Takahashi ⬤ https://orcid.org/0000-0002-8278-2688
Hiroyuki Fujishiro ⬤ https://orcid.org/0000-0003-1483-835X
Mark D Ainslie ⬤ https://orcid.org/0000-0003-0466-3680

References

[1] McPherson A and DeLucas L J 2015 Microgravity protein crystallization *NPJ Microgravity* **1** 15010

[2] Imura T, Nakagawa K, Kawahara Y and Yuge L 2018 Stem cell culture in microgravity and its application in cell-based therapy *Stem Cells Dev.* **27** 1298–302

[3] Beaugnon E and Tournier R 2003 Levitation of organic materials *Nature* **349** 470

[4] Nikolayev V S, Chatain D, Beysens D and Pichavant G 2011 Magnetic gravity compensation *Microgravity Sci. Technol.* **23** 113–22

[5] Wada H *et al* 2012 Application of high-field superconducting magnet to protein crystallization *Phys. Procedia Technol.* **36** 953–7

[6] Durrell J H, Ainslie M D, Zhou D, Vanderbemden P, Bradshaw T, Speller S, Filipenko M and Cardwell D A 2018 Bulk superconductors: a roadmap to applications *Supercond. Sci. Technol.* **31** 103501

[7] Durrell J H *et al* 2014 A trapped field of 17.6 T in melt-processed, bulk Gd-Ba-Cu-O reinforced with shrink-fit steel *Supercond. Sci. Technol.* **27** 082001

[8] Huang K *et al* 2020 Composite stacks for reliable >17 T trapped fields in bulk superconductor magnets *Supercond. Sci. Technol.* **33** 02LT01

[9] Vakaliuk O, Werfel F, Jaroszynski J and Halbedel B 2020 Trapped field potential of commercial Y-Ba-Cu-O bulk superconductors designed for applications *Supercond. Sci. Technol.* **33** 095005

[10] Ainslie M D and Fujishiro H 2019 *Numerical Modelling of Bulk Superconductor Magnetization. IOP Expanding Physics* (Bristol: IOP Publishing)

[11] Takahashi K, Fujishiro H and Ainslie M D 2018 A new concept of a hybrid trapped field magnet lens *Supercond. Sci. Technol.* **31** 044005

[12] Takahashi K, Fujishiro H and Ainslie M D 2020 Simulation study for magnetic levitation in pure water exploiting the ultra-high magnetic field gradient product of a hybrid trapped field magnet lens (HTFML) *J. Appl. Phys.* **127** 185106

[13] Namba S, Fujishiro H, Naito T, Ainslie M D and Takahashi K 2019 Experimental realization of a hybrid trapped field magnet lens using a GdBaCuO magnetic lens and MgB_2 bulk cylinder *Supercond. Sci. Technol.* **32** 12LT03

[14] Yin D-C 2015 Protein crystallization in a magnetic field *Prog. Cryst. Growth Charact. Mater.* **61** 1–26

[15] Kobayashi T, Mori T, Akiyama Y, Mishima F and Nishijima S 2017 Study on separation of structural isomer with magneto-Archimedes method *J. Phys.: Conf. Ser.* **897** 012018

[16] Miura O, Yamagishi K and Yamamoto D 2018 Magneto-Archimedes levitation of precious metals under a high magnetic field gradient *J. Phys.: Conf. Ser.* **1054** 012086

[17] Ren Y, Weinstein R, Liu J, Sawh R P and Foster C 1995 Damage caused by magnetic pressure at high trapped field in quasi-permanent magnets composed of melt-textured Y-Ba-Cu-O superconductor *Physica* C **251** 15–26

[18] Yanagi Y, Yoshikawa M, Itoh Y, Oka T, Ikuta H and Mizutani U 2004 Generation of extremely strong magnetic fields in open space by using metal-ring-reinforced 60 mmφ Sm-Ba-Cu-O superconducting bulk *Physica* C **412–414** 744–9

[19] Miyamoto T, Nagashima K, Sakai N and Murakami M 2000 Direct measurements of mechanical properties for large-grain bulk superconductors *Physica* C **340** 41–50

[20] Fujishiro H, Naito T, Yanagi Y, Itoh Y and Nakamura T 2019 Promising effects of a new *hat structure* and double metal ring for mechanical reinforcement of a REBaCuO ring-shaped bulk during field-cooled magnetization at 10T without fracture *Supercond. Sci. Technol.* **32** 065001

[21] Fujishiro H, Takahashi K, Naito T, Yanagi Y, Itoh Y and Nakamura T 2018 New proposal of mechanical reinforcement structures to annular REBaCuO bulk magnet for compact and cryogen-free NMR spectrometer *Physica* C **550** 52–56

[22] Jirsa M, Pust L, Dlouhý D and Koblischka M R 1997 Fishtail shape in the magnetic hysteresis loop for superconductors: interplay between different pinning mechanisms *Phys. Rev.* B **55** 3276–84

[23] Kii T *et al* 2012 Low-temperature operation of a bulk HTSC staggered array undulator *IEEE Trans. Appl. Supercond.* **22** 4100904

[24] Ikezoe Y, Kaihatsu T, Sakae D, Uetake H, Hirota N and Kitazawa K 2002 Separation of feeble magnetic particles with magneto-Archimedes levitation *Energy Convers. Manage.* **43** 417–25

[25] Ramachandran N and Leslie F W 2005 Using magnetic fields to control convection during protein crystallization-analysis and validation studies *J. Cryst. Growth* **274** 297–306

[26] Yan E-K, Zhang C-Y, He J and Yin D-C 2016 An overview of hardware for protein crystallization in a magnetic field *Int. J. Mol. Sci.* **17** 1906

[27] Zhao P, Xie J, Gu F, Sharmin N, Hall P and Fu J 2018 Separation of mixed waste plastics via magnetic levitation *Waste Manag.* **76** 46–54

[28] Mirica K A, Shevkoplyas S S, Phillips S T, Gupta M and Whitesides G M 2009 Measuring densities of solids and liquids using magnetic levitation: fundamentals *J. Am. Chem. Soc.* **131** 10049–58

[29] Tomita M and Murakami M 2003 High-temperature superconductor bulk magnets that can trap magnetic fields of over 17 Tesla at 29 K *Nature* **421** 517–20

[30] Namba S, Fujishiro H, Ainslie M D, Takahashi K, Namburi D K, Zhou D and Naito T 2019 Design optimization of a hybrid trapped field magnet lens (HTFML) *IEEE Trans. Appl. Supercond.* **29** 6801605

[31] Namba S, Fujishiro H, Naito T, Ainslie M D and Huang K Y 2019 Electromagnetic strain measurements and two-directional mechanical stress estimation for a REBaCuO ring bulk reinforced by a metal ring during field-cooled magnetization *Supercond. Sci. Technol.* **32** 125001

[32] Katagiri K, Murakami A, Shoji Y, Teshima H, Sawamura M, Iwamoto A, Mito T and Murakami M 2004 Tensile and bending mechanical properties of bulk superconductors at room temperature *Physica* C **412–414** 633–7

[33] Kan R, Katagiri K, Murakami A, Kasaba K, Shoji Y, Noto K, Sakai N and Murakami M 2004 Deformation and fracture behavior of SM123 bulk superconductors by compressive loading at room temperature *IEEE Trans. Appl. Supercond.* **14** 1114–7